

Perpendicular ferromagnetic resonance measurements of damping and Landé g -factor in sputtered $(\text{Co}_2\text{Mn})_{1-x}\text{Ge}_x$ thin films

H. T. Nembach,¹ T. J. Silva,¹ J. M. Shaw,¹ M. L. Schneider,² M. J. Carey,³ S. Maat,³ and J. R. Childress³

¹National Institute of Standards and Technology (NIST), 325 Broadway, Boulder, Colorado 80301

²University of Montana, Dept. of Physics and Astronomy, Missoula, Montana 59812

³Hitachi Global Storage Technologies, 3403 Yerba Buena Road, San Jose, California 95135

(Received 3 September 2010; revised manuscript received 8 April 2011; published 8 August 2011)

X-ray diffraction (XRD), magnetometry, and ferromagnetic resonance (FMR) measurements were performed on sputtered thin films of the nominal Heusler alloy $(\text{Co}_2\text{Mn})_{1-x}\text{Ge}_x$ with varying Ge content and annealing temperatures. XRD indicates some degree of B2 alloy formation, with strong (110) texturing. FMR measurements were performed in a perpendicular geometry that minimized the contribution of two-magnon scattering to the linewidth. The FMR data indicate a significant increase in linewidth for samples that lack a well-defined (220) peak, presumably as a result of inhomogeneous line broadening. Samples annealed at 200 °C exhibit decreasing Landau–Lifshitz damping with increasing Ge content, while samples annealed at 245 and 300 °C have a nonlinear dependence of linewidth on frequency. The nonlinear component of the linewidth data was successfully fit with a generalized theory of slowly relaxing impurities, originally proposed by Van Vleck and Orbach. The modified theory includes the possibility of transverse coherence during the relaxation process. Magnetometry and FMR spectroscopy results were analyzed in the context of Malozemoff’s generalized Slater–Pauling (GSP) theory, with the conclusion that the Ge sites support a significant negative-polarized spin density of several tens of percent. The GSP analysis results were consistent with a more conventional analysis of the spectroscopic g -factor that is appropriate for alloys. The proportionality of the strength of the slow-relaxer contribution to the damping suggests that the negatively polarized Ge atoms are acting as the slowly relaxing impurities in question.

DOI: [10.1103/PhysRevB.84.054424](https://doi.org/10.1103/PhysRevB.84.054424)

PACS number(s): 76.50.+g, 75.50.Ss, 75.30.Hx

I. INTRODUCTION

Heusler alloys¹ have received considerable attention in recent years because many of these compounds are half-metallic; i.e., the majority spin band is conductive and the minority is insulating.^{2,3} As a result, these materials have a theoretical 100% spin polarization at the Fermi level at low temperatures. Materials with such high spin polarization have significant potential for spintronics applications; Heusler alloys have been successfully employed as electrodes for spin injectors and tunneling magnetoresistance (TMR) devices.^{4–8} Read sensors in hard disk drives (HDDs) currently utilize the TMR effect, but current-perpendicular-to-plane (CPP) giant magnetoresistance (GMR) read sensors are an attractive alternative, due to the intrinsic lower resistance of the all-metallic CPP-GMR geometry when sensor dimensions are less than 50 nm.⁹ It is proposed that the signal-to-noise ratio of nanoscale CPP-GMR read heads could be greater than that of nanoscale TMR heads if high spin-polarization materials, (e.g., half-metallic Heusler alloys,) can be utilized as the magnetic layers of the spin-valve sensor.^{10–12} Of the various Heusler alloys currently under consideration, Co_2MnGe has a number of properties that make it very practical for such applications: (1) A predicted spin-polarization of 100% at low temperatures,^{13–15} (2) a substantial bulk saturation magnetization of $\mu_0 M_s \cong 1.2$ T; (3) A high Curie temperature of $T_c = 905$ K;¹⁶ (4) a low postdeposition annealing temperature for the inducement of a ferromagnetic phase. There have been several recent reports of ferromagnetic resonance (FMR),^{17–22} Brillouin light scattering,²⁰ and time-resolved magneto-optic Kerr effect^{23,24} measurements by use of both full- and half-Heusler alloys. In Ref. 21, Mizukami *et al.* reported that the Landau–Lifshitz damping parameter α was as small as 0.001 for sputtered Co_2FeAl . Similarly, a recent theoret-

ical calculation based on magnon-electron scattering theory predicts $\alpha = 1.9 \times 10^{-4}$ for Co_2MnGe .²⁵ Such low damping is particularly undesirable for CPP-GMR read heads, where weak damping promotes spin-torque-induced noise.⁹ Because of this last consideration, it is important to characterize and possibly even engineer damping in the Heusler alloys intended for HDD applications.

We studied $(\text{Co}_2\text{Mn})_{1-x}\text{Ge}_x$ (CMG) for a range of Ge contents and three different postdeposition annealing temperatures. Annealing was necessary to promote sufficient crystallinity for ferromagnetic order to arise. In general, we assume that higher annealing temperatures are more likely to promote the desired $L2_1$ phase of the Heusler alloys, and we will present evidence for some degree of $L2_1$ order obtained with a combination of magnetometry and x-ray diffraction (XRD) data. Perpendicular ferromagnetic resonance (P-FMR) measurements with a saturating magnetic bias field pointing out of the film plane were carried out over a frequency range of 1 to 40 GHz in order to study the damping in this material. This geometry was chosen to minimize the contribution of two-magnon scattering to the measured linewidth.²⁶ We find that the field-swept linewidth vs. frequency exhibits a bump-like nonlinearity at intermediate frequencies for certain compositions and annealing temperature. We successfully fit the data with the model of slowly relaxing impurities, originally proposed by Van Vleck and Orbach,²⁷ though we needed to generalize the model to include the possibility of coherence during the impurity-relaxation process. Fitting the spectroscopic data in a manner that is self-consistent with the presumption of slow-relaxer damping, we also find that the spectroscopic g -factor decreases in value with increasing Ge content for the higher annealing temperatures, eventually falling below a value of 2. Two methods of analysis that rely on spectroscopic and/or magnetometry data provide

strong evidence that the dependence of both M_s and g on increasing Ge can be attributed to a significant density of antiferromagnetically aligned spins on the Ge sites. Correlation of the slow-relaxer damping with Ge content points to the spin-polarized Ge as the slowly relaxing impurities in question, perhaps in the form of either substitutional or interstitial point defects that would occur with greater likelihood as the Ge content increases.

II. SAMPLE PREPARATION AND CHARACTERIZATION

Polycrystalline CMG samples with varying Ge contents were prepared by DC magnetron sputtering on glass substrates. First, a buffer layer of Ta (5 nm)/Cu (5 nm) was deposited, followed by 7.5-nm CMG. Finally the samples were capped with Cu (5 nm)/Ta (5 nm). Samples were annealed after deposition at 200, 245, and 300 °C for 5 h. The fractional atomic percentage content of Ge, n_{Ge} , ranged from $n_{Ge} = 0.20$ to $n_{Ge} = 0.32$ in steps of $\Delta n_{Ge} = 0.02$. The nominal Heusler stoichiometry was $n_{Ge} = 0.25$.

The saturation magnetic moment of each sample was measured at room temperature with a conventional vibrating-sample magnetometer (VSM), which we present in Fig. 1. The magnetometer-applied field was swept between ± 1.8 T for the determination of the sample moment in a fully saturated state, and the data were corrected for the diamagnetic moment of the sample holder. The VSM was calibrated before measuring each sample using a 100-nm-thick Ni film standard with a known moment at 1% precision. Film thicknesses were calibrated to within 1.3% accuracy using x-ray reflectometry. Examples of hysteresis loop data are presented in Fig. 2 for a subset of the 200 and 300 °C annealed samples. From the hysteresis data, we find that all the films were fully saturated for applied fields > 0.4 T. Variable-temperature measurements with a SQUID magnetometer on a subset of the samples (not shown) confirmed that the change in the magnetic moment between 300 and 4 K was negligible, as expected for a material with a Curie temperature well in excess of room temperature. For the 245 and 300 °C annealed samples, M_s linearly decreases with increasing Ge content, ranging between 900 and 600 kA/m ($\mu_0 M_s = 1.13$ to 0.75 T). For comparison, the room temperature bulk moment of Co_2MnGe was reported

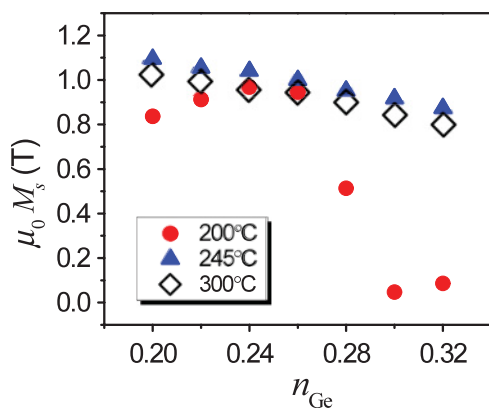


FIG. 1. (Color online) Saturation magnetization density M_s for all prepared samples with varying Ge content n_{Ge} and postdeposition annealing temperature, as determined with a VSM.

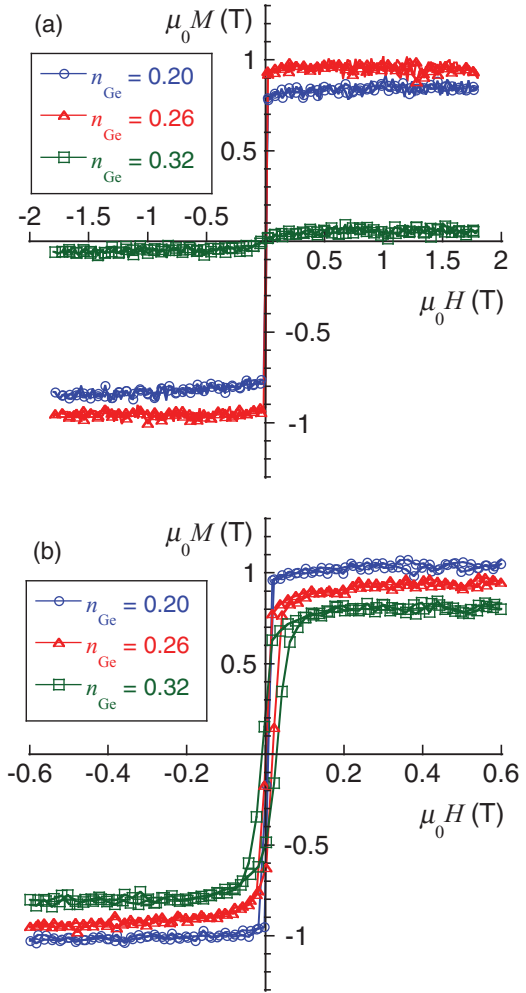


FIG. 2. (Color online) Hysteresis loop data for the (a) 200 °C and (b) 300 °C annealed samples with $n_{Ge} = 0.20$ (blue open circles), 0.26 (red open triangles), and 0.32 (green open squares). The full data sets used to determine M_s were obtained by use of a swept applied field between -1.8 and 1.8 T. The presented data for 300 °C (b) annealed samples cover a limited field range of only -0.6 and 0.6 T solely for the purposes of demonstrating the effect of variable Ge content on coercivity and saturation field, both of which increase with increasing Ge content.

to be 960 kA/m (1.2 T).¹⁶ For the 200 °C annealed films, M_s has a maximum at $n_{Ge} = 0.24$, followed by a sharp reduction in the moment at $n_{Ge} = 0.28$ and a collapse of room-temperature magnetic order of almost 100% for $n_{Ge} \geq 0.3$.

To put our magnetometry results in the context of previous work in this field, Ishikawa *et al.* obtained a magnetization of $\mu_0 M_s = 1$ T for L_{21} -ordered, epitaxial, 45-nm Co_2MnGe films grown on (001) MgO and annealed at 400 °C. In the study by Rajanikanth *et al.*, of 50-nm sputtered thin-film Co_2MnGe grown on thermally oxidized Si substrates with confirmed L_{21} order, postanneal magnetization values ranged from $\mu_0 M_s = 0.86$ T (300 °C anneal) to $\mu_0 M_s = 1.19$ T (500 °C anneal).²⁸ However, films with magnetization $\mu_0 M_s < 0.86$ T in the same study were found to exhibit significant disorder. We conclude that the magnetization values measured for most of our 245 and 300 °C annealed films are consistent with those expected for thin films with a substantial degree of L_{21} order. (Only

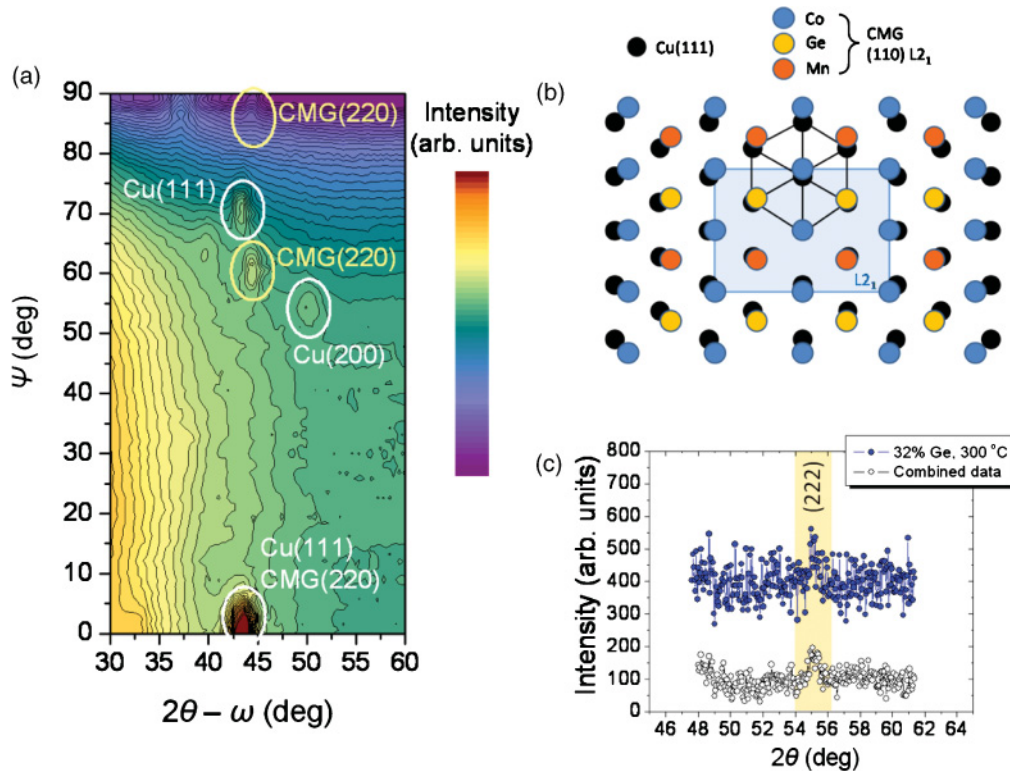


FIG. 3. (Color online) (a) Contour plot of the two-axis XRD data for the 200°C anneal, $n_{\text{Ge}} = 0.24$ sample. The film normal direction is $\psi = 0^\circ$. The CMG (220) peaks are circled, as well as the Cu (111) and (200) peaks. The CMG (220) peak can occur in numerous phases of Co_2MnGe , including the B2 and L_{21} phases. (b) A proposed model for how (111) Cu would act as a highly strained template for the growth of either B2- or L_{21} -ordered Co_2MnGe . (c) XRD data showing the presence of the (222) diffraction peak at $\psi = 90^\circ$, $2\theta = 55^\circ$ for higher-temperature anneal samples. The blue filled circles are data for the 300°C annealed sample with $n_{\text{Ge}} = 0.32$. The open black circles are an average of $\psi = 90^\circ$ scans for all 245 and 300°C annealed samples with $n_{\text{Ge}} \geq 0.24$.

the $n_{\text{Ge}} = 0.32$, 300°C anneal sample was found to have a magnetization of less than 0.86 T.)

The nonmonotonic behavior of the magnetization for the 200°C annealed samples is most likely the result of one or more phase transitions between unspecified crystal ordered states when the annealing temperature is below that required for formation of the B2 and/or L_{21} phase. Indeed, temperature-dependent measurements of magnetic moment during the anneal of 40-nm-thick films (not shown) indicate that an irreversible structural change does not occur until annealed at 236°C in the case of stoichiometrically correct Co_2MnGe .²⁹

Two-axis XRD scans with Cu $K\alpha$ radiation were used to ascertain the presence of crystalline order in the CMG layer after annealing. (220) diffraction peaks were observed for most of the samples at $\psi = 0^\circ, 60^\circ, 90^\circ$; $2\theta = 44^\circ$, as expected for either the B2 or L_{21} phases of CMG with a (110) texture. An example of two-axis scan data, in the form of a contour plot, is shown in Fig. 3(a) for the $n_{\text{Ge}} = 0.24$ sample annealed at 200°C. (For this plot and all subsequent discussion, we define $\psi = 0^\circ$ as normal to the film surface.) Also shown in the same plot are the Cu (111) and (200) peaks associated with a (111) textured Cu film. However, a (220) diffraction peak was not observed for the 200°C annealed films with $n_{\text{Ge}} \geq 0.3$. Peak-fitting analysis of the (220) peak at $\psi = 90^\circ$; $2\theta = 44^\circ$ was used to determine the in-plane lattice constant a , with results in the range $0.5795 \text{ nm} > a > 0.5765 \text{ nm}$. The lattice constant decreases approximately linearly by 0.5% with increasing Ge

content for samples annealed at all temperatures. The nominal bulk lattice parameter for the L_{21} phase of Co_2MnGe is $a = 0.5743 \text{ nm}$.¹⁶ Thus, almost all samples exhibited tensile, in-plane strain varying from 0.4% to 0.9%. The linear reduction in the lattice constant with increasing Ge content could be understood in terms of the smaller atomic size of Ge, which is 7% smaller than Co and 11% smaller than Mn.

We present a simple schematic in Fig. 3(b) to show how the CMG (220) surface would match with the Cu (111) surface. Within this model, the degree of lattice mismatch (8% – 13%) between the two surfaces presumably yields a proliferation of dislocations at the film interfaces, which significantly relaxes the resultant strain.

We note that the (220) peak is insensitive to elemental site-swapping disorder for the L_{21} phase; i.e., a (220) peak would also be present for either the B2 phase, in which only the Mn and Ge atoms are randomly interchanged, or the bcc solid-solution phase, in which all three constituent species are randomly intermixed throughout the lattice.³⁰ (We note that, in the case of the B2 or bcc solid-solution phases, the correct index of the measured peak would be for diffraction from the (110) plane.)

The presence of a B2 and/or L_{21} order was confirmed for samples annealed at 245 and 300°C with $n_{\text{Ge}} \geq 0.24$ via detection of a weak CMG (220) diffraction peak at $\psi = 90^\circ$; $2\theta = 55^\circ$. The (222) diffraction peak was not detected for any of the samples annealed at 200°C. An example of the (222)

peak for the 300 °C, $n_{\text{Ge}} = 0.32$ sample is shown in Fig. 3(c), along with an average of all $\psi = 90^\circ$ scans for samples with $n_{\text{Ge}} \geq 0.24$. While the signal-to-noise ratio for the single scan with $n_{\text{Ge}} = 0.32$ is marginal for detection of the (222) peak, the average of the scans clearly shows the presence of the peak indicative of either L2₁ or B2 order. The (311) plane diffraction peak required for L2₁ order at $\psi = 90^\circ$; $2\theta = 53^\circ$ was not detected for any of the samples. [Given the structure factor for the (311) reflection,¹⁶ that particular peak is forbidden if the samples are composed purely of the B2 phase.³⁰] However, the absence of a detectable (311) peak is not proof of the absence of L2₁ order; it is very possible that the (311) peak is simply too small to detect in the case of such small film thicknesses. Indeed, previous studies of sputtered CMG thin films of a similar thickness have not yielded a (311) XRD peak in spite of substantial evidence that L2₁ order was indeed present.^{28,31,32}

The absence of a detectable (222) diffraction peak for any of the 200 °C annealed samples, along with the independent observation of a significant irreversible enhancement of magnetic moment for CMG films when annealed above 236 °C (not shown here)²⁹ leads us to conclude that annealing at 200 °C is insufficient to form an ordered phase that is any more than a simple bcc solid solution.

The putative (220) peak at $\psi = 0^\circ$; $2\theta = 44^\circ$ is of significantly reduced amplitude for $n_{\text{Ge}} = 0.28$ for the 200 °C annealed samples and is no longer detectable for $n_{\text{Ge}} \geq 0.3$. For the 245 and 300 °C annealed samples, the (220) peak starts to drop significantly in amplitude relative to the Cu (111) peak at $\psi = 0^\circ$; $2\theta = 43^\circ$ for $n_{\text{Ge}} \geq 0.3$ and $n_{\text{Ge}} \geq 0.26$, respectively. This suggests that an excessive Ge content eventually leads to either a reduction or complete absence of order for the CMG films, although other processes such as a transition to an alternate phase cannot be strictly excluded. We also note that the near absence of a room-temperature moment in the 200 °C anneal films coincides with the absence of any XRD signal from the nominal (220) plane.

We should emphasize that the observation of XRD peaks associated with B2 and/or L2₁ ordering does not imply that the entire sample is ordered. It signifies only some fractional presence of such ordering in the samples. A determination of the degree of ordering requires substantially more measurements.³³

III. FERROMAGNETIC RESONANCE MEASUREMENT TECHNIQUE

A broadband FMR spectrometer based on the vector network analyzer (VNA) FMR technique^{34–37} was used to measure the resonance frequency and the linewidth in the P-FMR geometry; a static out-of-plane magnetic field as high as $\mu_0 H = 2.35$ T, sufficient to saturate the magnetization out of the film plane, was applied to the sample. A variable in-plane microwave field with a frequency range between 0.01 and 40 GHz was applied to the sample via a coplanar waveguide with a 100- μm -wide center conductor. Before being placed face down on the waveguide, samples were spin-coated with less than 1 μm of a protective, nonconducting poly(methyl methacrylate) (PMMA) layer to avoid shorting of the waveguide. The complex transmission parameter S_{21} was

measured with a VNA at a fixed frequency while the external magnetic field was swept.

To analyze the data, we assume the general understanding that the complex reflection parameter S_{11} and the complex transmission parameter S_{21} can be broken into magnetic and nonmagnetic contributions, where ΔS_{11} and ΔS_{21} are the magnetic contributions to the reflection and transmission parameters, respectively, and S_{11}^0 and S_{21}^0 are the nonmagnetic contributions. We then make the following definitions to relate the magnetic and nonmagnetic contributions, with $S_{11}^1 \doteq S_{11}^0 + \Delta S_{11}$ and $S_{21}^1 \doteq S_{21}^0 + \Delta S_{21}$. We then employ the following analytical relationship between the complex susceptibility $\chi(H)$ and the S parameters, as derived in Ref. 36:

$$\chi(H) = \chi_0 \left(\frac{1 + S_{11}^1 - S_{21}^1}{1 - S_{11}^1} - \frac{1 + S_{11}^0 - S_{21}^0}{1 - S_{11}^0} \right), \quad (1)$$

where χ_0 is an imaginary function of the experimental parameters, such as frequency and film thickness. (We refer the reader to Ref. 36 to find the details concerning χ_0 .) In the limit of weak reflection of microwave power from the sample (i.e., $|S_{11}| \ll 1$), the complex susceptibility can be reduced to

$$\chi(H) \cong \chi_0 [(2 + 2S_{11}^0 - S_{21}^0)\Delta S_{11} - (1 + S_{11}^0)\Delta S_{21}]. \quad (2)$$

In the quasi-static limit, we can show that $\Delta S_{11} = -\Delta S_{21}$,³⁵ and we can further simplify Eq. (2) to

$$\chi(H) \cong -\chi_0 (3(1 + S_{11}^0) - S_{21}^0)\Delta S_{21}. \quad (3)$$

Note that we obtain the intuitively satisfying result of $\chi(H) \cong -2\chi_0\Delta S_{21}$ from Eq. (3) in the limit of 100% transmission of the microwave excitations, i.e., with perfect impedance matching between the waveguide and measurement system when the magnetic contribution has been nullified by either raising the temperature above the Curie temperature or by saturating the magnetization parallel to the direction of the linearly polarized microwave field.

In this particular study, we are not interested in the amplitude of the susceptibility. As such, it is easiest in practice to extract the resonance field and the linewidth for each excitation frequency by simply fitting the S_{21} data to the complex function

$$S_{21}(H, t) = S_{21}^0 + Dt - \frac{\chi(H)}{\tilde{\chi}_0}, \quad (4)$$

where D is a purely phenomenological complex, first-order correction for the time-dependent drift of the measurement electronics, and $\tilde{\chi}_0 \doteq \chi_0(3(1 + S_{11}^0) - S_{21}^0)$. We found in practice that signal drift was a nonnegligible quantity and that minimization of the empirical quantity D , as well as the presumption of applicability of a simple linear correction, required a rapid sweep rate of the applied magnetic field.

The susceptibility is derived from the Landau–Lifshitz equation.³⁸ For the perpendicular geometry, $\chi(H)$ is given by

$$\chi(H) = \frac{M_{\text{eff}}(H - M_{\text{eff}})}{(H - M_{\text{eff}})^2 - H_{\text{eff}}^2 - i\frac{\Delta H}{2}(H - M_{\text{eff}})}, \quad (5)$$

where $H_{\text{eff}} \doteq 2\pi f/(\gamma\mu_0)$ and $M_{\text{eff}} = M_s - H_k^\perp$. In Eq. (5), the microwave frequency is f , μ_0 is the permeability of free

space, M_s is the saturation magnetization, H_K^\perp is the out-of-plane anisotropy field, ΔH is the full-width-half-maximum (FWHM) linewidth, $\gamma \doteq (g\mu_B)/\hbar$ is the gyromagnetic ratio, g is the Landé spectroscopic splitting factor, μ_B is the Bohr magneton, and \hbar is the reduced Planck's constant.

The procedure to determine linewidth ΔH , the resonance field H_{res} , and the effective magnetization M_{eff} from S_{21} measurements involves several steps: (1) We set $g = 2$ in order to calculate H_{eff} . (We have verified that setting $g = 2$ does not influence any of the final results for H_{res} and ΔH , provided we use $g = 2$ in step 3 as well); (2) S_{21} is fitted to Eq. (1) with the following eight fitting parameters: $|S_{21}^0|$, $\arg(S_{21}^0)$, $|D|$, $\arg(D)$, $|\tilde{\chi}_0|$, $\arg(\tilde{\chi}_0)$, M_{eff} , and ΔH ; 3) the resonant field H_{res} is determined for each excitation frequency f by use of the Kittel equation for this perpendicular geometry:

$$H_{\text{res}} = \frac{2\pi f}{|\gamma| \mu_0} + M_{\text{eff}}. \quad (6)$$

For this step, we assign $g = 2$, as in step 1, to eliminate any influence of the choice of g on H_{res} ; 4) H_{res} vs. f is fitted with the Kittel equation, Eq. (6), but this time with g and M_{eff} as the fitting parameters, where the slope is proportional to $1/g$ and the y-axis intercept is equal to $-M_{\text{eff}}$. The uncertainties of the fitted results were obtained by means of the standard method for the determination of confidence limits on estimated parameters for nonlinear models under the assumption of Gaussian white noise, whereby we rely on the inversion of the calculated curvature matrix to estimate the covariance matrix of the standard errors in the fitted parameters.³⁹

We wish to emphasize that use of Eq. (6) to fit our FMR data does not rely on prior knowledge of M_s for the samples in question. Both the spectroscopic splitting factor g and M_{eff} are fully determined by fitting of the FMR field data with Eq. (6).

In the framework of the Landau-Lifshitz model for damping by itself, the linewidth depends linearly on the product of the excitation frequency and the phenomenological damping parameter α , with an expected zero-frequency intercept of zero. In general, a nonzero intercept ΔH_0 is experimentally observed, which is usually attributed to an inhomogeneity of the local resonance field.⁴⁰ Thus, following common practice, we can fit ΔH at each frequency with the function

$$\Delta H = \frac{4\pi\alpha f}{|\gamma| \mu_0} + \Delta H_0, \quad (7)$$

which is then used to extract α and ΔH_0 from the linewidth vs. frequency data.

IV. EXPERIMENTAL RESULTS

A. 200 °C anneal

In Fig. 4(a), we present ΔH as a function of f for the samples that were annealed at 200 °C with $n_{\text{Ge}} < 0.28$. The overall slope of ΔH vs. f is clearly decreasing with increasing Ge content up to $n_{\text{Ge}} = 0.26$. Figure 4(b) shows the fitted values of ΔH_0 and α from the data of Fig. 4(a). Values of α decrease with increasing Ge content down to a minimum value of 0.0042 ± 0.0007 for $n_{\text{Ge}} = 0.26$. (The nominal damping for $n_{\text{Ge}} = 0.28$ is even smaller, with $\alpha \cong 0.0025$, but with substantially greater uncertainty, for reasons that will be discussed below.)

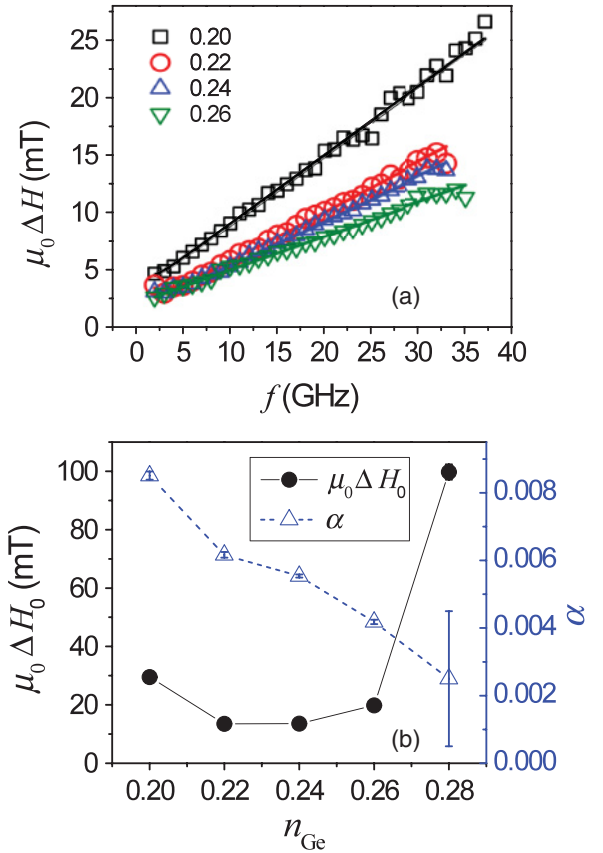


FIG. 4. (Color online) (a) FMR linewidth as a function of frequency for the 200 °C sample series. Shown are linewidths for four different amounts of Ge content in the range of $0.20 \leq n_{\text{Ge}} \leq 0.28$. The dependence on frequency is linear, with decreasing slope as the Ge content increases. (b) Landau-Lifshitz damping parameter α and inhomogeneous broadening ΔH_0 for the 200 °C sample series as a function of Ge content.

The inhomogeneous linewidth broadening shown in Fig. 4(b) drops somewhat from $n_{\text{Ge}} = 0.20$ to 0.22 and then remains at about $\mu_0 \Delta H_0 \cong 20$ mT until $n_{\text{Ge}} = 0.28$, whereupon the inhomogeneous broadening rapidly grows to almost 100 mT. The reduction of α with increasing Ge content up to $n_{\text{Ge}} = 0.26$ is evocative of similar experimental findings for the B2-ordered alloy²² CoFeGe and is indeed in qualitative agreement with theories that predict very small values for the damping parameter for the case of true half-metallic Heusler alloys of Co_2MnGe and Co_2MnSi ,²⁵ insofar as a prerequisite for the formation of a Heusler alloy is the correct stoichiometric ratios of the constituent species. However, the smallest value of damping reported here for 200 °C is still considerably larger than the theoretically predicted values for CMG.

The omission in Fig. 4 of the data for samples with $n_{\text{Ge}} > 0.26$ Ge is explained as follows. Figure 5 shows the measured real part of S_{21} for a Ge content of $n_{\text{Ge}} = 0.26$ [Fig. 5(a)] and 0.28 [Fig. 5(b)] to illustrate the sudden and strong broadening of the linewidth when the Ge content is increased from $n_{\text{Ge}} = 0.26$ to $n_{\text{Ge}} = 0.28$. For $n_{\text{Ge}} = 0.28$, the extracted inhomogeneous linewidth is $\mu_0 \Delta H_0 = (94.7 \pm 2.6)$ mT. ΔH_0 is even broader for samples with higher Ge content. Thus we excluded the data for $n_{\text{Ge}} > 0.28$ from Figs. 4

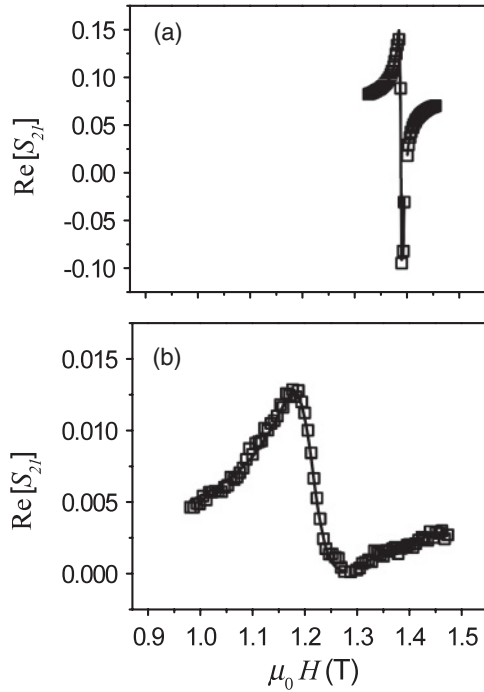


FIG. 5. (a) The real part of S_{21} for the 200 °C sample with $n_{\text{Ge}} = 0.26$, and (b) the real part of S_{21} for the 200 °C sample with $n_{\text{Ge}} = 0.28$. The values of S_{21} have been adjusted to remove offsets and linear drift. Comparison of the two data sets illustrates how the linewidth of the spectra broadens very suddenly with only a 2% increase in Ge content.

and 6 because the large linewidths led to unacceptably large uncertainties in the fitted values for α , M_{eff} , and g .

We note that the onset of the large linewidths for the 200 °C annealed samples for $n_{\text{Ge}} \geq 0.28$ coincides with the apparent rapid reduction and eventual loss of both the magnetic moment and the presumed disordering of CMG with increasing Ge content, as observed in the XRD data, suggesting that the linewidth broadening is potentially the result of diminished crystalline order.

Data for M_{eff} and g vs. Ge content for the 200 °C annealed samples are shown in Fig. 6. We find that g is greater than 2 for all the data presented, with an average value of $\langle g \rangle = 2.028 \pm 0.006$, where the uncertainty is simply the statistical standard deviation. In Fig. 6, $\mu_0 M_{\text{eff}}$ displays a maximum of 0.98 T at $n_{\text{Ge}} = 0.24$, with a sudden drop of almost 20% for $n_{\text{Ge}} = 0.28$.

B. 245 °C anneal

The samples annealed at 245 °C show a significantly different behavior for ΔH vs. f . In Fig. 7, we present ΔH vs. f data for samples annealed at 245 °C with Figs. 7(a), 7(b), and 7(c) showing the data for $n_{\text{Ge}} = 0.20$, 0.28, and 0.30, respectively. Over the range of measured frequencies, we find that the linewidth exhibits richer behavior than the expected linear dependence predicted by Eq. (4). In the low-frequency range, the linewidth *increases* sharply with *decreasing* frequency. At intermediate frequencies, we observe a *broad yet distinct bump* in the linewidth for $n_{\text{Ge}} > 0.22$.

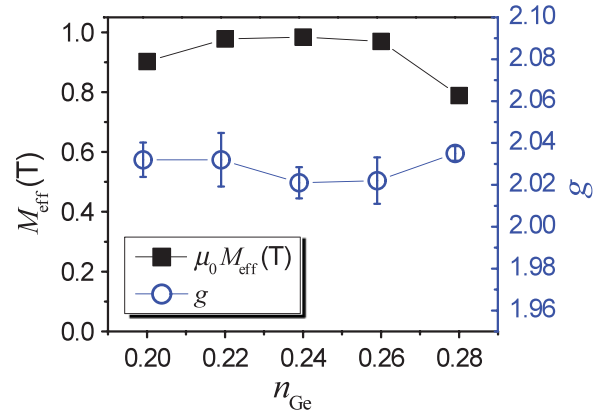


FIG. 6. (Color online) Spectroscopic quantities $\mu_0 M_{\text{eff}}$ and g as functions of Ge content for the 200 °C sample series.

Nonlinearities in linewidth vs. frequency data that have the qualitative appearance of peaks have been previously observed in films of yttrium iron garnet (YIG).⁴¹ The previously observed peaks in YIG were attributed to the slow-relaxing impurity mechanism, whereby damping is facilitated by the thermally driven longitudinal relaxation of an impurity atom that is exchange-coupled to the ferromagnetic lattice.²⁷ The exchange coupling gives rise to an “exchange anisotropy,” whereby the splitting of a particular thermally occupied energy level of the impurity depends on the instantaneous direction of the magnetization. Note that the thermally driven repopulation of the dynamically fluctuating energy level in accordance with the demands of Boltzmann statistics results in damping of the ferromagnetic precession.⁴² In the original encounter with slow-relaxer damping, first observed experimentally by Dillon and Nielsen in 1959,⁴³ and eventually explained by Van Vleck and Orbach,²⁷ the relaxation is mediated by the exchange-induced anisotropy of the two lowest-energy levels of rare-earth ions in YIG. More recently, the theory was successfully extended to explain the dependence of damping in rare-earth-doped Permalloy ($\text{Ni}_{81}\text{Fe}_{19}$) films on rare earth concentration and temperature.⁴⁴ Indeed, we refer the reader to Ref. 44 for an excellent review of the underlying physics behind the slow-relaxing impurity mechanism.

The thermal relaxation of the impurity level results in an effective fluctuating magnetic field that acts on the ferromagnetic moment with an autocorrelation function given by

$$\langle h(t_0)h(t_0 + t) \rangle = \begin{cases} \langle h^2 \rangle e^{-t/\tau}; & t \geq 0 \\ 0; & t < 0 \end{cases}, \quad (8)$$

where τ is the thermal-relaxation time for exchange-mediated dopant energy levels and $\langle h^2 \rangle$ is the variance of the field fluctuations. From fluctuation-dissipation theory,^{45–47} the frequency response of the damping associated with such field fluctuations is obtained by Fourier transform of the autocorrelation function:^{48–50}

$$\alpha(\omega) = \left[\frac{|\gamma| \mu_0^2 M_s V}{2k_B T} \right] \langle h^2 \rangle \int_{-\infty}^{\infty} D(t) e^{-i\omega t} dt, \quad (9)$$

where $D(t) \doteq \langle h(t_0)h(t_0 + t) \rangle / \langle h^2 \rangle$ and V is the volume of the affected macrospin. In the specific case of a slow-relaxing

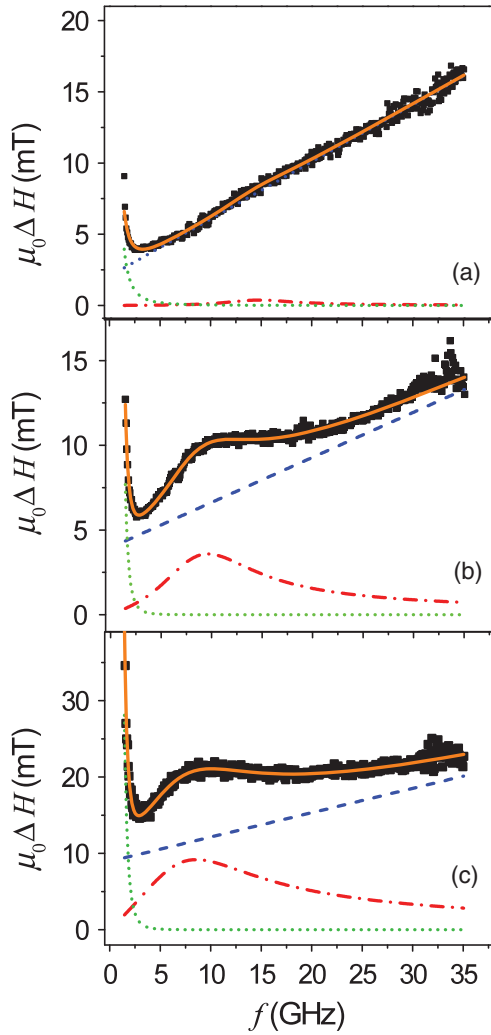


FIG. 7. (Color online) Linewidth data for the 245°C sample series, with (a) $n_{\text{Ge}} = 0.20$, (b) $n_{\text{Ge}} = 0.28$, and (c) $n_{\text{Ge}} = 0.30$. Black squares are the measured data points, and the orange solid curves are the fit to Eq. (13). The contributions of the different terms in Eq. (13) are shown as the dotted (green) line for the low field loss, the dashed (blue) line for the Landau-Lifshitz damping plus inhomogeneity, and the dot-dashed (red) line for the “generalized” slow-relaxing impurity loss.

impurity-relaxation mechanism, the frequency-domain damping is given by

$$\alpha_{\text{slow}}(\omega) = CF(T) \left[\frac{\tau}{1 + (\omega\tau)^2} - i \frac{\omega\tau^2}{1 + (\omega\tau)^2} \right], \quad (10)$$

where

$$C = \frac{|\gamma|N_{\text{slow}}}{8M_s k_B T} \left[\left(\frac{\partial E_{\text{slow}}}{\partial \phi} \right)^2 + \left(\frac{\partial E_{\text{slow}}}{\partial \theta} \right)^2 \right], \quad (11)$$

$$F(T) = \text{sech}^2 \left(\frac{E_{\text{slow}}}{k_B T} \right). \quad (12)$$

N_{slow} is the concentration of slow-relaxing impurities, k_B is Boltzmann’s constant, T is temperature, and E_{slow} is the spin splitting of the impurity ion. The angular derivatives of E_{slow} (where θ and ϕ are the inclination and azimuth

polar coordinate angles, respectively, as typically defined) reflect the anisotropic exchange coupling of the impurity with the ferromagnetic moment. We note that C has units of inverse seconds.⁻¹ The real part of Eq. (10) is the effective Landau-Lifshitz-like damping parameter with an associated FWHM linewidth $\Delta H_{\text{slow}} \doteq 4\pi \text{Re}(\alpha_{\text{slow}}) f / (|\gamma| \mu_0)$, and the imaginary part is proportional to the shift of the resonance field δH , where $\delta H \doteq 2\pi \text{Im}(\alpha_{\text{slow}}) f / |\gamma| \mu_0$. [We note that there appears to be a typographical error in Ref. 44, wherein an erroneous positive sign is ascribed to the imaginary part of Eq. (10)]. In Ref. 44, it was presumed that $\omega\tau \ll 1$ over the entire range of frequencies employed for FMR, precluding the ability to observe a peak in linewidth vs. frequency. However, if $\omega\tau \approx 1$ in the measurement range of FMR, Eq. (10) predicts the occurrence of a peak in the linewidth.

We used Eq. (10), together with the conventional Landau-Lifshitz model of Eq. (7) and a power-law term $\propto f^{-n}$ for the low-field losses, to fit our linewidth data for the samples annealed at 245 and 300°C:

$$\begin{aligned} \Delta H(f) = \Delta H_0 + \frac{4\pi f}{|\gamma| \mu_0} (\alpha + \text{Re}(\alpha_{\text{slow}}(2\pi f))) \\ + \Delta H_{\text{low}} \left(\frac{\text{Hz}}{f} \right)^n. \end{aligned} \quad (13)$$

While the fits were adequate, given the signal-to-noise ratio of the data, we also found that the fits yielded unphysically small values for the inhomogeneous broadening ΔH_0 , with fits often returning values of $\Delta H_0 = 0$. (Fitting yielded $\Delta H_0 = 0$ for $n_{\text{Ge}} = 0.26, 0.28, 0.30$ with the 245°C annealed samples, as well as the samples annealed at 300°C with $n_{\text{Ge}} = 0.20, 0.22, \text{ and } 0.24$, to be discussed later.) However, the observation of strong low-field losses for both the high-concentration Ge samples in the 245°C series and all of the samples annealed at 300°C is inconsistent with the hypothesis of negligible inhomogeneity. Indeed, low-field losses result when the applied field is insufficient to fully saturate the magnetization, as occurs when there is a strong spatial variation of the local anisotropy, which leads to inhomogeneous broadening as a consequence.

In the case of standard “slow-relaxer” theory, the peak in the linewidth is not the result of a peak in the damping parameter itself. Instead, α_{slow} is a maximum at $f = 0$, and the peak in the linewidth is a mathematical consequence of the fact that linewidth is the product of frequency and a function that is a Lorentzian, centered at zero. (Physically, this describes the competition during the damping process between the relaxation mechanism, which tends to keep the dopant electronic system in thermal equilibrium, and the precession process, which tends to disrupt the electronic system out of thermal equilibrium.) Careful observation of the presented linewidth data suggested to us that the peak in the linewidth may actually be a result of a peak in α_{slow} for $f > 0$. Such a peak could occur in the context of slow-relaxer theory if we allow for a more general consideration of coherence in the slowly relaxing impurity, to be explained below.

Let us suppose that the relaxation rate of the impurity ion was sufficiently slow such that $\tau \geq 1/\omega_0$, where ω_0 is the

natural oscillation frequency of the exchange-coupled impurity spin. In this case, the autocorrelation of the field fluctuations

would need to be generalized to account for the occurrence of transient coherence in the impurity-relaxation process:

$$\langle h(t_0)h(t_0 + t) \rangle = h_0^2 \cos(\omega_0 t) e^{-t/\tau}. \quad (14)$$

The resultant functional form for the damping would now be

$$\tilde{\alpha}_{\text{slow}}(\omega) = CF(T)\tau \left\{ \frac{((\omega_0\tau)^2 + (\omega\tau)^2 + 1) + i(\omega\tau)[(\omega_0\tau)^2 - (\omega\tau)^2 - 1]}{[(\omega_0\tau)^2 - (\omega\tau)^2]^2 + 2[(\omega_0\tau)^2 + (\omega\tau)^2] + 1} \right\}, \quad (15)$$

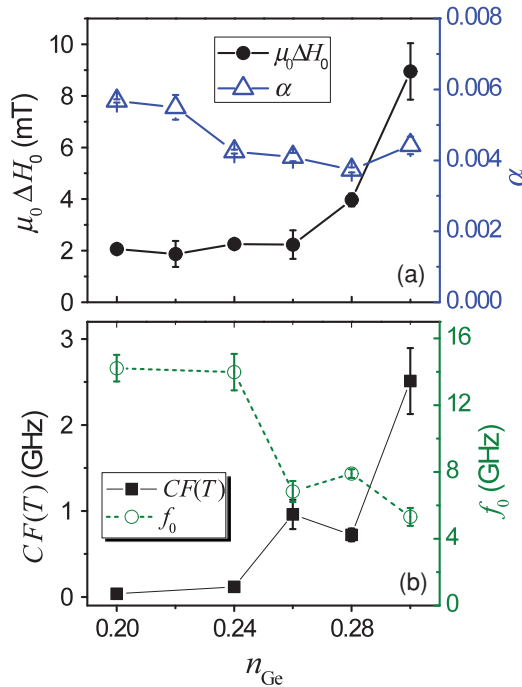


FIG. 8. (Color online) Linewidth fitting results for the 245 °C sample series. (a) Landau-Lifshitz damping parameter α and inhomogeneous broadening ΔH_0 vs. Ge content. (b) Amplitude $CF(T)$ and coherence frequency f_0 of slow-relaxing impurity damping vs. Ge content.

where the tilde over α_{slow} signifies the more general form for the impurity-driven damping term. This generalized slow-relaxer damping is equivalent to the more specific theory in the limit $\omega_0\tau \rightarrow 0$.

The real part of Eq. (15) has a maximum near $\omega = \omega_0$. When applied to the fitting of the linewidth data by substituting $\tilde{\alpha}_{\text{slow}}(\omega)$ for $\alpha_{\text{slow}}(\omega)$ in Eq. (14) for the 245 and 300 °C annealed samples, Eq. (15) was found to yield superior fits with significantly reduced residues and consistently nonzero values for ΔH_0 (with the exception of one particular sample, discussed in more detail below). Some of the fitting results for the 245 °C sample are shown in Figs. 7(a), 7(b), and 7(c), where we also show the relative contributions of the various parts in Eq. (13) [with the aforementioned substitution $\alpha_{\text{slow}}(\omega) \rightarrow \tilde{\alpha}_{\text{slow}}(\omega)$] to the overall linewidth. The dotted (green) line is the low-field loss, the dashed (blue) line is the Landau-Lifshitz damping plus inhomogeneous broadening,

and the dot-dashed (red) line is the generalized slow-relaxing impurity loss. The sum of all terms is shown by the solid line (orange), which agrees very well with the measured linewidth.

The low-field-loss exponent n was allowed to float in the fitting process. The fitted values varied from between 2.6 and 4.7, with a mean of 3.7 and a standard deviation of 0.9. In the theory for low-field loss, the linewidth broadening is ascribed to details of the hysteretic process by which domain formation occurs when the applied field is insufficient to fully saturate the sample.⁵¹ While it is beyond the scope of this paper to fully explain the low-field-loss contribution to the measured linewidth in our samples, we believe the invocation of low-field loss to be sufficiently credible to warrant the use of a power-law term in the fitting procedure to model the linewidth behavior at low frequencies. However, modification of the details of the fitting at low frequencies had only a weak effect on the fitted values for α and the slow-relaxer parameters.

For the case of the 245 °C annealed sample with $n_{\text{Ge}} = 0.22$, the application of the generalized slow-relaxer model resulted in excessive error bars for almost all the fitted parameters. Since we observe no peak in the field-swept linewidth for that particular sample, we reverted to fitting with the conventional linewidth model of Eq. (7) for that particular sample.

In Fig. 8(a), we show the fitted Landau-Lifshitz damping coefficient α and the inhomogeneous linewidth broadening ΔH_0 for all the samples annealed at 245 °C except for $n_{\text{Ge}} = 0.32$. (There is a substantial increase in the estimated error of the fitting process for the largest Ge content of $n_{\text{Ge}} = 0.32$ due to the extremely large linewidth measured at that Ge concentration.) The inhomogeneous broadening $\mu_0 \Delta H_0$ is less than 2.5 mT for $n_{\text{Ge}} \leq 0.26$ and steadily increases by almost a factor of 6 (14 mT) for larger n_{Ge} . The damping α starts at 0.0057 for $n_{\text{Ge}} = 0.20$, then steadily decreases with increasing Ge content up to $n_{\text{Ge}} = 0.28$ ($\alpha = 0.0037 \pm 0.0001$), beyond which α increases, albeit slightly. For samples with $n_{\text{Ge}} \geq 0.26$, the generalized slow-relaxer contribution is significant and the amplitude $CF(T)$ increases strongly from frequencies less than 0.1 GHz to almost 3 GHz with increasing Ge content. The coherence frequency $f_0 \doteq \omega_0/2\pi$ decreases from ~ 14 to 3 GHz over the same range of n_{Ge} , as shown in Fig. 8(b). The fitted impurity-relaxation time τ (not shown) varies between 20 and 30 ps without any systematic trend with varying n_{Ge} . We note that the substantial increase in the inhomogeneous broadening is somewhat correlated with the onset of the putative slow-relaxer damping mechanism for this sample series.

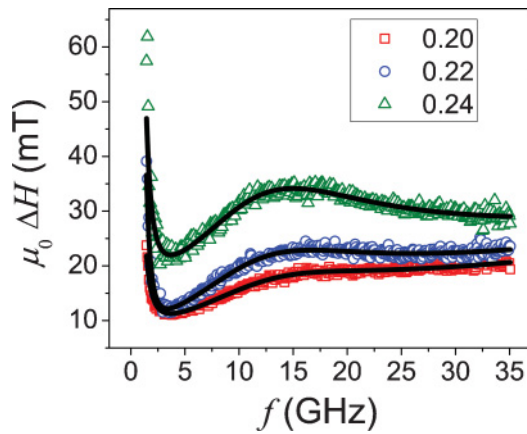


FIG. 9. (Color online) Linewidth data for the 300°C sample series, with $n_{\text{Ge}} = 0.20$ (red open squares), $n_{\text{Ge}} = 0.22$ (blue open circles), and $n_{\text{Ge}} = 0.24$ (green open triangles). Fits according to Eq. (13) are shown as solid (black) lines through the data.

C. 300°C anneal

The samples annealed at 300°C show linewidth behavior very similar to those annealed at 245°C, though over a more limited range of Ge content, as shown in Fig. 9. For $n_{\text{Ge}} \geq 0.26$ the linewidth again incurs a substantial increase, similar to what was observed in the samples annealed at 200°C with $n_{\text{Ge}} \geq 0.28$ and at 245°C with $n_{\text{Ge}} = 0.32$. Again, the jump in the linewidth with increasing Ge content coincides with the point at which XRD data indicate a significant diminution of the presumptive (220) diffraction peak, suggesting a loss of texturing with excessive Ge content. Just as we found for the 200 and 245°C samples, the strong enhancement in the linewidth also resulted in significant uncertainty in the fitted values for M_{eff} , g , and α , so we omit the $n_{\text{Ge}} \geq 0.26$ data from our analysis. In Fig. 9, the measured linewidth is shown together with a fit of the data to Eq. (13). Again, we found that the additional damping terms associated with low-field loss and the generalized slow-relaxer model adequately account for the deviation from the Gilbert damping behavior, with similar qualitative results as a function of increasing Ge content. The extracted values for $\mu_0 \Delta H_0$ and α are presented in Fig. 10(a). $\mu_0 \Delta H_0$ starts at 7.5 mT for $n_{\text{Ge}} = 0.20$, then rises up to 15 mT for $n_{\text{Ge}} = 0.24$. Conversely, α starts at 0.0039 for $n_{\text{Ge}} = 0.20$, then eventually drops to $\alpha = 0.0026 \pm 0.0003$ for $n_{\text{Ge}} = 0.24$, which was the smallest value of damping observed for all the samples we measured. The slow-relaxer contribution to the linewidth was substantial for all three of the 300°C samples that were analyzed, with $CF(T)$ increasing almost linearly with increasing n_{Ge} from 1.6 to approximately 4 GHz, as shown in Fig. 10(b). The coherence frequency f_0 changed only slightly with n_{Ge} , varying within the frequency range of 10–11 GHz. The relaxation time τ (not shown) was about half of that in the case of the 245°C annealed samples, varying between 15 and 17 ps.

V. SELF-CONSISTENT SPECTROSCOPIC ANALYSIS

Unlike the case of the data set for the 200°C anneal, we could not simply use the Kittel equation [Eq. (6)] to extract

the spectroscopic parameters g and M_{eff} for the 245 and 300°C data; to be consistent with the slow-relaxer model, we needed to adjust the fitting process for the spectroscopic data of resonance field vs. frequency in accordance with the imaginary part of Eq. (15), which describes the purely reactive influence of the slowly relaxing impurities on the magnetization. We found that the predicted variations in the resonant field given by the imaginary part of Eq. (15) were too small in comparison with the magnitude of the applied field to permit direct fitting against the reactive part of the generalized slow-relaxer model. Instead, with Eq. (13), we used the extracted values from the fits of the linewidth data to inform the use of the imaginary part of Eq. (15) as a correction of the field-swept spectroscopy data, which were then fitted to the Kittel equation, Eq. (6). The corrected, self-consistent values for $\mu_0 M_{\text{eff}}$ in the case of the 200, 245, and 300°C sample series are presented in Fig. 11. For the 245°C series shown in Fig. 11, $\mu_0 M_{\text{eff}}$ steadily decreases with increasing Ge content, starting at a little over 1 T and ending just above 0.8 T. Similarly, in the case of the 300°C samples, $\mu_0 M_{\text{eff}}$ started at 1.08 T for $n_{\text{Ge}} = 0.20$ and ended just above 1 T for $n_{\text{Ge}} = 0.24$. A similar trend was observed for the spectroscopic g -factor, shown in Fig. 12, with g dropping with increasing n_{Ge} from 2.02 to just over 1.98 in the 245°C series, while g drops from 1.97 to a little over 1.94 in the 300°C series. A weighted linear fit of the data for g suggests the functional form of $g = 2.08 - 0.30 \cdot n_{\text{Ge}}$ for the 245°C sample series, and $g = 2.17 - 1.08 \cdot n_{\text{Ge}}$ for the 300°C sample series. As a point of comparison, the same linear regression for the 200°C sample series (also shown in Fig. 12) yields $g = 2.0092 + 0.086 \cdot n_{\text{Ge}}$.

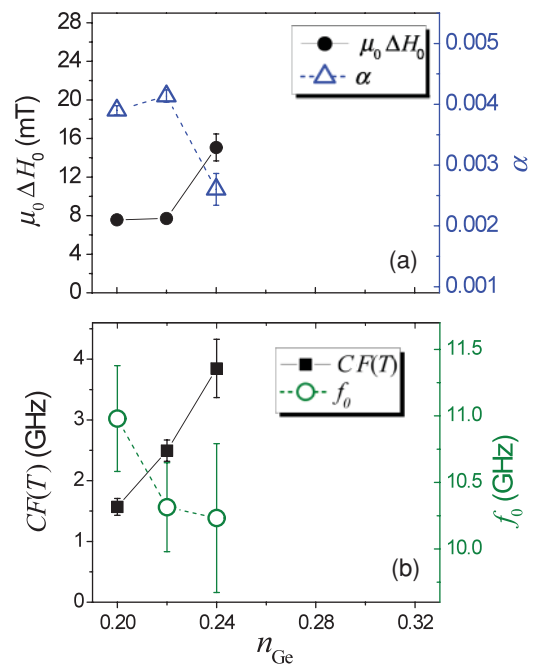


FIG. 10. (Color online) Linewidth fitting results for the 300°C sample series. (a) Landau-Lifshitz damping parameter α and inhomogeneous broadening ΔH_0 vs. Ge content. (b) Amplitude $CF(T)$ and coherence frequency f_0 of slow-relaxing impurity damping vs. Ge content.

VI. DISCUSSION

Similar nonlinearities in ΔH vs. f have been reported for FMR measurements of other Heusler alloys, including sputtered Co_2FeAl ²¹ and CoFeGe ²² films. In both of these cited cases, *nonlinearities were observed with the saturating magnetic field oriented in the film plane*, while in Ref. 22 linear behavior was observed for out-of-plane measurements. In both cases, the observed nonlinearities were attributed to two-magnon scattering. However, for the P-FMR geometry employed for our particular study, *in which the applied field points out of the film plane, the contribution of two-magnon scattering to the linewidth should be minimal*; the frequency of the spin-wave band increases monotonically with increasing wavenumber in such a geometry, thereby excluding the possibility of any modes that are degenerate with the FMR.

Some magnons can still be generated by the uniform magnetization precession caused by the finite linewidth of the resonance and the spin-wave modes resulting from Landau–Lifshitz-like damping processes, which in turn results in nonzero overlap of the initial and final states.²⁶ Since the frequency-swept linewidth is linearly proportional to excitation frequency for P-FMR, we expect the two-magnon contribution to the field-swept linewidth would also be linear in frequency to first order, thereby simply adding to the measured value of the damping parameter.

We can exclude nonlinear three- and four-magnon processes as the source of the nonlinearity of the linewidth because we verified that the effect does not depend on excitation amplitude. This is to be expected because of the absence of available degenerate spin-wave states that would fulfill the momentum and energy conservation simultaneously, as discussed above.

Having fitted our data in the context of both conventional Landau–Lifshitz theory and a generalized form of the slow-relaxer theory, we find that the smallest values of α for these particular films (300 °C anneal, $n_{\text{Ge}} = 0.24$) is less by about a factor of 2 than what we obtained with Permalloy films of a similar thickness in the P-FMR geometry ($\alpha = 0.0054 \pm 0.0001$). A small value of α for CMG is of concern for the application of such alloys for HDD applications.²⁵ The

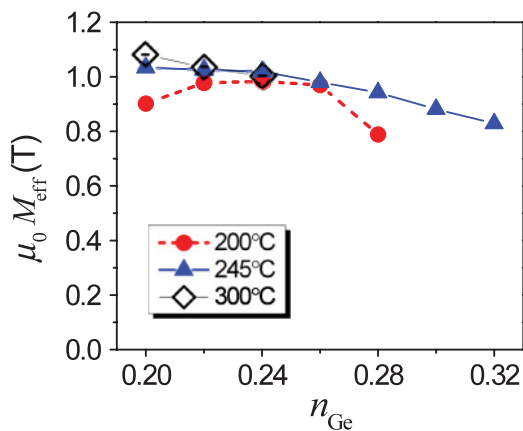


FIG. 11. (Color online) Self-consistent values for $\mu_0 M_{\text{eff}}$ for all three annealing temperatures. Data for the 245 and 300 °C anneals were corrected for the reactive part of the slow-relaxer damping process, as formulated in the imaginary part of Eq. (15).

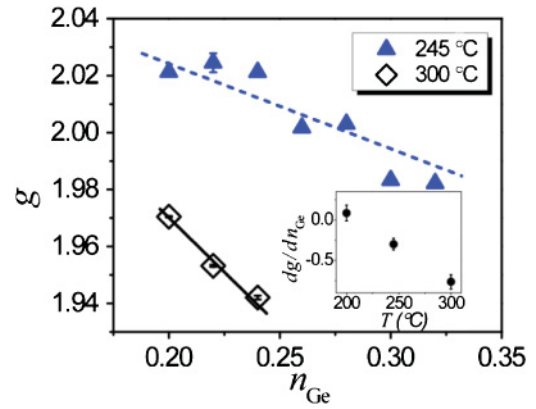


FIG. 12. (Color online) Self-consistent values of the spectroscopic g -factor for the 245 and 300 °C annealed samples, including fits with linear regression. Data were corrected for the reactive part of the slow-relaxer damping process, as formulated in the imaginary part of Eq. (15). Inset shows the approximated slope from linear regression of g vs. n_{Ge} as a function of the annealing temperature.

discrepancy between our data and theory may indicate that our samples are not completely half-metallic, though analysis of our data in the context of generalized Slater Pauling (GSP) theory (presented below) does confirm that the Fermi surface is located in a deep minimum (if not a complete bandgap) within the density of states (DOS) for the minority band.

Another source of discrepancy between our data and theoretical predictions for damping in CMG may be the result of spin pumping. In the spin-pumping mechanism, transverse components of spin are driven from the ferromagnetic film into any sandwiching nonmagnetic metallic film via a peristaltic-pumping action.^{52,53} This pumping of transverse spin, in turn, acts to damp the ferromagnetic precession in the magnetic film. Measurements of the spin-pumping contribution to damping in 5-nm NiFe films indicate that the enhancement of the measured damping can be as large as 0.0016 due to spin pumping through a single metallic interface with Cu.⁵⁴ If we assume for the sake of comparison only that the spin-mixing conductance for NiFe–Cu and CMG–Cu is the same, we then estimate that the spin-pumping contribution to the measured damping in 7.5-nm CMG films would be 0.0021. Such a contribution would be a substantial correction to the measured values presented here. Indeed, such a correction would imply that the smallest intrinsic damping that we observed might be as small as $\alpha = 6.3 \times 10^{-4}$. However, until appropriate spin-pumping measurements have been performed to determine the spin-mixing conductance of the CMG–Cu interface, we emphasize that the damping values reported here must be treated as upper bounds for the intrinsic damping that would be measured in the absence of any spin-pumping effects.

The presence of an additional damping mechanism, albeit one with a strong frequency dependence, implies the possibility of engineering the total damping in such alloys once we understand the physical mechanism that underlies the observed enhancement of the FMR linewidth. Fitting of our data to the model for a slow-relaxing impurity raises the question as to the particular impurity acting on the magnetic moment of CMG. In the case of the 245 °C annealed samples, we find

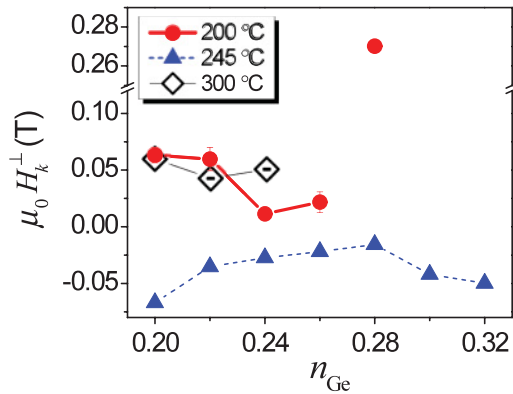


FIG. 13. (Color online) Perpendicular anisotropy H_k^\perp as a function of Ge content for all three annealing temperature series. The anisotropy is negative for the 245 °C anneal series, indicative of easy-plane anisotropy, and positive for the 200 and 300 °C series.

that the reduction of the spectroscopic g -factor below 2 at approximately $n_{\text{Ge}} \approx 0.28$ is correlated with the onset of the slow-relaxer damping mechanism, as well as the threshold for both the loss of (220) texturing and the increase of the inhomogeneous broadening. This would seem to suggest that the metalloid component of the sputtered alloy and its effect on the crystal structure of the film might play important roles in determining the dynamical properties of this particular alloy.

It is well known that the spectroscopic g -factor is proportional to the total average magnetic moment per uncompensated spin for the compound in question. The total moment includes any orbital contributions that are the result of spin-orbit coupling (SOC). (SOC is the only available mechanism for orbital moment in solids with cubic symmetry, given that the crystal field quenches any orbital moment that might be otherwise present for isolated atoms.) As such, we expect $g > 2$ for crystalline ferromagnetic solids, as is generally observed. Thus the observation of $g < 2$ is a surprising result that is not easily explained in the context of conventional FMR theory.

In Fig. 12, we show a plot of g vs. Ge content for the 245 and 300 °C annealed samples on a single plot. Higher anneal temperatures appear to reduce the slope of g vs. n_{Ge} , dg/dn_{Ge} . In the inset of Fig. 11, we show dg/dn_{Ge} as a function of anneal temperature, indicating a linear dependence of the slope on the annealing temperature over the range we have explored in this study. The implication is that Ge is in some way responsible for the partial compensation of the magnetic moment of the 245 and 300 °C sample series (i.e., more Ge reduces the moment per spin, which is proportional to g), though without significantly altering the average number of spins in the formula unit. Such compensatory behavior has been observed for rare-earth and transition-metal intermetallic alloys.^{55,56} Theory has shown that Ge should indeed contribute a negative moment to the magnetization in a perfect $L2_1$ structure.⁵⁷ However, the calculated moment of Ge ($\sim 0.07 \mu_B$) is very modest and unlikely to cause the scale of effects observed here. While the data are insufficient to draw any firm conclusions, either interstitial or substitutional defects of Ge may possibly carry a much stronger negative moment. For example, a substitutional defect of Ge at a Co site would incur a much different exchange overlap with neighboring

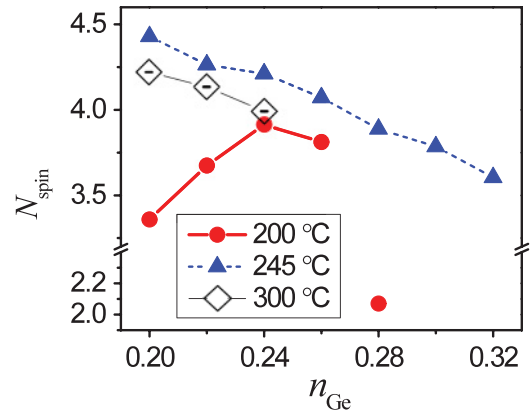


FIG. 14. (Color online) Spin density per f.u. N_{spin} as a function of Ge content for all three annealing series. The spin density near the ideal stoichiometry of $n_{\text{Ge}} = 0.25$ is $N_{\text{spin}} \cong 4.0 \pm 0.1$. This is 20% less than the generally accepted bulk value of approximately $N_{\text{spin}} \cong 5$.

Co atoms, thereby having a very different resultant moment. Hence, such Ge point defects could also reasonably be the slow-relaxing “impurities” responsible for the observed frequency dependence of the linewidth. Further evidence for a negative moment associated with the Ge sites is presented below.

Having data for M_s , M_{eff} , and g , we are now able to determine both the perpendicular anisotropy H_k^\perp and the spin density N for our samples. The perpendicular anisotropy is given by $H_k^\perp = M_s - M_{\text{eff}}$. Figure 13 is a plot of H_k^\perp vs. Ge content for all three anneal series. The perpendicular anisotropy was found to be negative for the 245 °C annealed samples (easy-plane anisotropy), with values ranging from -20 to -70 mT, and positive (easy-axis anisotropy) for the 200 and 300 °C annealed samples, with a similar range for the magnitude of H_k^\perp , with the sole exception of the $n_{\text{Ge}} = 0.28/200$ °C annealed sample, where the anisotropy is in excess of 0.25 T. For both the 200 and 245 °C annealed samples, the magnitude of the anisotropy appears to be minimized within a couple percent of the “ideal” Heusler stoichiometry of $n_{\text{Ge}} = 0.25$.

To calculate the spin density N , we begin with the definition of the g -factor as being proportional to the average magnetic moment per uncompensated electron in the material:

$$N = \frac{2M_s}{g\mu_B}, \quad (16)$$

where M_s is the volume density of the magnetic moment, as determined by magnetometry. Because there are four atoms per unit cell in the case of Co_2MnGe , we can conveniently consider the spin density per formula unit N_{spin} :

$$N_{\text{spin}} \doteq N \frac{a^3}{4} = \frac{M_s a^3}{2g\mu_B}. \quad (17)$$

A plot of N_{spin} vs. n_{Ge} for the three different anneal temperatures is shown in Fig. 14. Except for the 200 °C samples, we find that N_{spin} tends to have a negative linear dependence on Ge content with a negative slope of approximately $dN/dn_{\text{Ge}} \approx -6.7$. In addition, we find that N_{spin} at the ideal Heusler stoichiometry of $n_{\text{Ge}} = 0.25$ is

approximately 20% less than what is expected for bulk Co_2MnGe .^{7,16}

Wurmehl *et al.*⁵⁸ and Fecher *et al.*⁵⁹ showed that the magnetic moment of the Co-based Heusler compounds follows closely to the GSP curve on the localized portion of the GSP curve where the average valence per atom Z satisfies $Z < 8$. Such behavior is indicative of a minority spin density that is relatively insensitive to changes in the alloy composition,⁶⁰ which is in turn a hallmark signature that the Fermi energy is near a deep minimum in the d -band DOS.⁶¹ According to the theory associated with the GSP curve in Ref. 38, the total number of uncompensated spins N_{spin} per formula unit (f.u.) is given by

$$N_{\text{spin}} = N_T \left[\sum_i n_i Z_i - 2 \sum_i n_i N_i^\downarrow \right], \quad (18)$$

where N_T is the total number of atoms in the f.u., $0 \leq n_i \leq 1$ is the fractional atomic concentration of the i th species per f.u., Z_i is the valence number for the i th species, and N_i^\downarrow is the composition-insensitive number of minority spins for the i th species usually associated with a nearly filled minority band DOS in strong ferromagnets. In the case of Co_2MnGe , the valence values are $Z = 9, 7,$ and 4 for Co, Mn, and Ge, respectively. Bulk measurements^{16,62} and calculations⁵⁷ have shown that the fixed number of minority spins for each species are approximately given by $N_{\text{Co}}^\downarrow \cong 4.1$, $N_{\text{Mn}}^\downarrow \cong 1.8$, and $N_{\text{Ge}}^\downarrow \cong 2$. Thus the net number of uncompensated spins per f.u. is expected to be $N_{\text{spin}} \cong 5$, with each Co contributing 0.8 spins, each Mn contributing 3.4 spins, and each Ge contributing zero spins. Residual deviations of the measured magnetic moment of Co_2MnGe from $5\mu_B$ per f.u. are usually attributed to the effects of SOC on the net effective moment per electron, i.e., $g \neq 2$.^{57,63} However, the data presented in Fig. 14 clearly indicate that our samples are missing the equivalent of an entire spin compared with accepted bulk values for Co_2MnGe .

If we assume that our samples are amenable to GSP curve analysis, we can make a further determination as to the relative responsibility of each atomic species for the apparent “missing spin”. For our particular case, we can rewrite Eq. (18) as

$$N_{\text{spin}} = N_T [n_{\text{Co}} Z_{\text{Co}} + n_{\text{Mn}} Z_{\text{Mn}} + n_{\text{Ge}} Z_{\text{Ge}} - 2[n_{\text{Co}} N_{\text{Co}}^\downarrow + n_{\text{Mn}} N_{\text{Mn}}^\downarrow + n_{\text{Ge}} N_{\text{Ge}}^\downarrow]]. \quad (19)$$

Since we vary only the Ge concentration while leaving the relative concentration of Co to Mn unchanged (i.e., $n_{\text{Co}} = 2n_{\text{Mn}}$), and we know that the total concentration must always obey $n_{\text{Co}} + n_{\text{Mn}} + n_{\text{Ge}} = 1$, we can rewrite Eq. (19) in terms of the Ge concentration alone:

$$N_{\text{spin}} = N_T \left[\frac{2}{3}(1-n_{\text{Ge}})Z_{\text{Co}} + \frac{1}{3}(1-n_{\text{Ge}})Z_{\text{Mn}} + n_{\text{Ge}}Z_{\text{Ge}} - 2 \left[\frac{2}{3}(1-n_{\text{Ge}})N_{\text{Co}}^\downarrow + \frac{1}{3}(1-n_{\text{Ge}})N_{\text{Mn}}^\downarrow + n_{\text{Ge}}N_{\text{Ge}}^\downarrow \right] \right]. \quad (20)$$

If we then take the derivative of Eq. (20) with respect to n_{Ge} , we obtain

$$\frac{dN_{\text{spin}}}{dn_{\text{Ge}}} = N_T \left[-\frac{1}{3}(2Z_{\text{Co}} + Z_{\text{Mn}}) + Z_{\text{Ge}} - 2 \left[-\frac{1}{3}(2N_{\text{Co}}^\downarrow + N_{\text{Mn}}^\downarrow) + N_{\text{Ge}}^\downarrow \right] \right]. \quad (21)$$

By use of the fact that $N_T = 4$ and the known valences for the constituent atoms, we obtain

$$[2N_{\text{Co}}^\downarrow + N_{\text{Mn}}^\downarrow - 3N_{\text{Ge}}^\downarrow] = \frac{13}{2} + \frac{3}{8} \frac{dN_{\text{spin}}}{dn_{\text{Ge}}}. \quad (22)$$

Using our magnetometry result of $N_{\text{spin}} \approx 4$ for $n_{\text{Ge}} = 0.25$, along with Eq. (20), we then determine that

$$[2N_{\text{Co}}^\downarrow + N_{\text{Mn}}^\downarrow + N_{\text{Ge}}^\downarrow] = \frac{25}{2}. \quad (23)$$

Combining Eqs. (22) and (23), we obtain

$$N_{\text{Ge}}^\downarrow = 3 \left[\frac{1}{2} - \frac{1}{32} \frac{dN_{\text{spin}}}{dn_{\text{Ge}}} \right]. \quad (24)$$

Substituting known values of the valence electron number and the experimentally measured slope $dN_{\text{spin}}/dn_{\text{Ge}} \approx -6.7$ into Eq. (24), we obtain $N_{\text{Ge}}^\downarrow \approx 2.125$ and $2N_{\text{Co}}^\downarrow + N_{\text{Mn}}^\downarrow = 10.375$ and, according to the rules of GSP theory, commensurate site-specific excess spin values of $s_{\text{Ge}} = Z_{\text{Ge}} - 2N_{\text{Ge}}^\downarrow \approx -0.25$ and $s_{\text{CoMn}} = 2Z_{\text{Co}} + Z_{\text{Mn}} - 2(2N_{\text{Co}}^\downarrow + N_{\text{Mn}}^\downarrow) \approx 4.25$. (We remind the reader that the nominal bulk values for Co_2MnGe are $2N_{\text{Co}}^\downarrow + N_{\text{Mn}}^\downarrow \approx 10$ and $N_{\text{Ge}}^\downarrow \approx 2$.)

While these calculations suggest that there is a 15% suppression of the spin population on the transition-metal sites relative to theoretical predictions, it implies a compensating inverted spin population at Ge sites of 0.25 minority spins that is particularly striking. While recent band structure calculations indeed lead to predictions of a nonzero negative spin density on the Ge sites, the theoretical values are of the order of only 0.065 spins or less,⁵⁷ as expected for the relatively small spin-orbit perturbation in this particular Heusler alloy. In our case, however, we note from the above analysis of our magnetometry data in the context of GSP theory that the Ge sublattice exhibits 4x greater antiferromagnetic (AF) moment than would generally be expected for this system.

An independent analysis of the spectroscopy data without reliance on the assumptions of GSP analysis also provides a means of estimating the spin polarization of the metalloid component in our samples. We begin by assuming that the net moments of the different constituent atoms of the alloy do not change when we vary the stoichiometry slightly about the ideal stoichiometric composition of Co_2MnGe . At the ideal Heusler stoichiometry, the joint moment of the Co and Mn atoms per f.u. and the moment of the Ge atoms per f.u. are given by $\tilde{\mu}_{\text{CoMn}}$, $\tilde{\mu}_{\text{Ge}}$, respectively, where the tilde denotes normalization by the Bohr magneton. As previously defined, the fractional number of Ge atoms in the alloy is n_{Ge} , and the total number of unpaired spins per f.u. at a given Ge content is parametrized by the function $N_{\text{spin}}(n_{\text{Ge}})$. We can then write the following equation for the spectroscopic splitting factor as a function of the Ge content:

$$g(n_{\text{Ge}}) = 2 \frac{\tilde{\mu}_{\text{CoMn}} \left(\frac{n_{\text{CoMn}}}{0.75} \right) + \tilde{\mu}_{\text{Ge}} \left(\frac{n_{\text{Ge}}}{0.25} \right)}{N_{\text{spin}}(n_{\text{Ge}})} \cong 2 \frac{\tilde{\mu}_{\text{CoMn}} \left(\frac{1-n_{\text{Ge}}}{0.75} \right) + \tilde{\mu}_{\text{Ge}} \left(\frac{n_{\text{Ge}}}{0.25} \right)}{N'_{\text{spin}} + \frac{dN_{\text{spin}}}{dn_{\text{Ge}}}(n_{\text{Ge}} - 0.25)} = \left(\frac{32}{3} \right) \frac{(N'_{\text{spin}} - \tilde{\mu}_{\text{Ge}})(1 - n_{\text{Ge}}) + 3\tilde{\mu}_{\text{Ge}}n_{\text{Ge}}}{4N'_{\text{spin}} + \frac{dN_{\text{spin}}}{dn_{\text{Ge}}}(4n_{\text{Ge}} - 1)}, \quad (25)$$

where we made use of our assumption that the total number of atoms per unit cell remains unchanged, i.e., $n_{\text{CoMn}} + n_{\text{Ge}} = 1$. The denominator describes how the number of spins in the formula unit changes with varying Ge content, and the numerator describes how the net moment of the f. u. depends on the relative contents of Co_2Mn and Ge. We approximated the denominator using a Taylor's series expansion in deriving the second line, with $N'_{\text{spin}} = N_{\text{spin}}(n_{\text{Ge}} = 0.25)$, and we made the substitution $\tilde{\mu}_{\text{CoMn}} = N'_{\text{spin}} - \tilde{\mu}_{\text{Ge}}$ in the third line. We then have the following equation describing the slope of g vs. n_{Ge} :

$$\frac{dg}{dn_{\text{Ge}}} = \frac{32}{3} \left\{ \left[\frac{4\tilde{\mu}_{\text{Ge}} - N'_{\text{spin}}}{(4N'_{\text{spin}} + \frac{dN_{\text{spin}}}{dn_{\text{Ge}}}(4n_{\text{Ge}} - 1))} \right] - 4 \frac{dN_{\text{spin}}}{dn_{\text{Ge}}} \left[\frac{(N'_{\text{spin}} - \tilde{\mu}_{\text{Ge}})(1 - n_{\text{Ge}}) + 3\tilde{\mu}_{\text{Ge}}n_{\text{Ge}}}{(4N'_{\text{spin}} + \frac{dN_{\text{spin}}}{dn_{\text{Ge}}}(4n_{\text{Ge}} - 1))^2} \right] \right\}. \quad (26)$$

We can now solve for $\tilde{\mu}_{\text{Ge}}$:

$$\begin{aligned} \tilde{\mu}_{\text{Ge}} = & \frac{1}{256N'_{\text{spin}}} \left[16 \left[3 \frac{dg}{dn_{\text{Ge}}} + 8 \right] N_{\text{spin}}^2 \right. \\ & + 24 \left[\frac{dg}{dn_{\text{Ge}}}(4n_{\text{Ge}} - 1) + 4 \right] N'_{\text{spin}} \frac{dN_{\text{spin}}}{dn_{\text{Ge}}} \\ & \left. + 3 \left[\frac{dg}{dn_{\text{Ge}}}(4n_{\text{Ge}} - 1)^2 \right] \left(\frac{dN_{\text{spin}}}{dn_{\text{Ge}}} \right)^2 \right]. \quad (27) \end{aligned}$$

For the measured values of $\frac{dg}{dn_{\text{Ge}}} = -0.30 \pm 0.07$ (see Fig. 12), $\frac{dN_{\text{spin}}}{dn_{\text{Ge}}} = -6.7$, and $N'_{\text{spin}} = 4.07$ for the 245 °C anneal series samples, we obtain $\tilde{\mu}_{\text{Ge}} = -0.35 \pm 0.03$. Alternatively, if we assume the theoretically expected value of $N'_{\text{spin}} = 5$ for the nominal Heusler alloy, disregarding the results of our magnetometry analysis for the moment, we obtain $\tilde{\mu}_{\text{Ge}} = -0.15 \pm 0.03$. For the 300 °C samples, if we use previously extracted values of $dg/dn_{\text{Ge}} \cong -0.76 \pm 0.09$, $dN_{\text{spin}}/dn_{\text{Ge}} \cong -6.0$, and $N'_{\text{spin}} \cong 3.95$, we find that $\tilde{\mu}_{\text{Ge}} \cong -0.42 \pm 0.03$. Alternatively, if we use $N'_{\text{spin}} = 5.0$, we then obtain $\tilde{\mu}_{\text{Ge}} \cong -0.23 \pm 0.04$. In all four cases, we find that the Ge atoms contribute a significant negative moment to the sample magnetization, providing qualitative confirmation of our GSP analysis results from which we concluded there was a significant negative spin polarization at the Ge sites. In the case of the 245 °C sample series, the extracted value for the spin density on the Ge sites from these estimates based on the dependence of g on Ge content is within 50% of the estimate obtained from the GSP analysis of the magnetometry data for the same samples. Thus both spectroscopy and magnetometry data concur in the indication that the Ge sites have a significant (of the order of several tens of percent) antiferromagnet-coupled spin polarization.

As the approximate calculations presented above have shown, the postulate of AF-ordered Ge atoms simultaneously explains the quantitative dependence of the total sample moment on Ge content for all but a few anomalous samples that were annealed at only 200 °C, as well as the dependence of g on the Ge content. However, the mechanism that would give rise to such significant ferrimagnetic order in our

samples is not yet clear. Nor is there sufficient supplementary experimental evidence to make an unambiguous determination concerning a Ge moment. Indeed, existent x-ray magnetic circular dichroism (XMCD) data for Co_2MnGe conflict as to whether there is a moment associated with Ge.^{62,64} We may very well conclude that our samples are sufficiently disordered as to not be amenable to a GSP analysis and that such an approach might be inherently flawed, thereby rendering our extracted values for Ge moment as erroneous. However, this does not explain why the analysis of the spectroscopic splitting factor also yields large negative moments on the Ge sites. In addition, films very similar to these may have been successfully used in nanoscale CPP-GMR heads, showing substantial improvements in signal levels in comparison with those fabricated with conventional transition-metal alloys.⁶⁵ Assuming as we might that the superior performance of Co_2MnGe as a head material implies a high degree of spin polarization, which concurrently implies that the Fermi energy is indeed located within a deep minimum of the minority band, if not a complete gap, we are then left with few alternatives to explain such unexpected spin ordering that are consistent with impressive performance at the device level. One possible explanation for the large negative moment due to Ge stems from the substantial strain in our films, as indicated from the XRD data. Alternatively, some of the Ge atoms may contribute to the formation of either interstitial or substitutional defects within the Co sublattice. Indeed, once the Ge content exceeds 25%, such defects are increasingly likely. For example, in a qualitative anomalous XRD study, which used a combinatorial epitaxial CMG film, a preponderance of vacancy defects was observed in the Co sublattice as the Ge content was increased beyond the ideal Heusler stoichiometry ($\sim 20\%$ Co vacancies for $n_{\text{Ge}} \cong 0.5$).³⁰ It is generally understood that ferromagnetic Heusler alloys can be treated as a composite of localized moments that are amenable to theoretical consideration with a Heisenberg Hamiltonian and that the exchange between the various moments is the result of indirect Rudermann-Kittel-Kasuya-Yosida- (RKKY-) type exchange via the mobile electrons within the system.² As such, we may suppose that either lattice strain or the occurrence of point defects might indeed induce a significant AF-coupled moment at the Ge sites.

The correlation of significant damping of the slow-relaxing impurity type for samples where $g < 2$, coupled with the earlier analysis of Ge moments, suggests that Ge point defects within the ordered crystal lattice might be the ‘‘impurity’’ responsible for the frequency-dependent component of the damping. The fact that the slow-relaxer damping was not observed in the samples annealed at only 200 °C suggests that crystal order beyond a simple bcc solid solution is also required for this specific damping mechanism since the samples in question did not exhibit a detectable (222) diffraction peak (otherwise indicative of $L2_1$ and/or $B2$ order) in the XRD analysis that was presented earlier.

The types of impurities that have been invoked in the past to explain slow-relaxing processes include rare-earth dopants in both insulating and metallic ferromagnets and various Fe cations that result from various defects in iron garnet films, including both Fe^{2+} and Fe^{4+} states.⁴¹ However, we are not aware of any previous studies investigating the possibility that

Ge atoms can act as relaxers in ferromagnetic metals, let alone potential half-metals.

In Fig. 8, we see that the strength of the slow-relaxer damping mechanism tends to increase with increasing Ge content for the 245 °C anneal series in the case of $n_{\text{Ge}} > 0.24$. A similar trend is seen in Fig. 10 for all of the 300 °C annealed samples that we have analyzed. Such proportionality suggests that excess Ge content beyond some temperature-dependent threshold level is leading to the formation of the slow-relaxing impurity sites. The slope of the dependence of the slow-relaxing damping strength in the quasi-linear regime is approximately $d(CF(T))/dn_{\text{Ge}} \cong 120$ GHz. Taking the derivative of Eq. (11) with respect to n_{Ge} , we obtain

$$\frac{dC}{dn_{\text{Ge}}} = \frac{|\gamma|E_{\text{ani}}^2}{8M_s k_B T} \frac{dN_{\text{slow}}}{dn_{\text{Ge}}}, \quad (28)$$

where $E_{\text{ani}} = [(\frac{\partial E_{\text{slow}}}{\partial \phi})^2 + (\frac{\partial E_{\text{slow}}}{\partial \theta})^2]^{1/2}$ is the anisotropy energy associated with the angular-dependent exchange perturbation of the impurity's electronic transition. Assuming that the energy gap of the absorbing impurity is insensitive to the Ge density, we can write

$$d(CF(T))/dn_{\text{Ge}} = \frac{|\gamma|E_{\text{ani}}^2}{8M_s k_B T} \frac{dN_{\text{slow}}}{dn_{\text{Ge}}} \text{sech}^2\left(\frac{E_{\text{slow}}}{k_B T}\right). \quad (29)$$

Now let's assume that all the Ge atoms in excess of 25% act as slow-relaxers (a specific example pertinent for the 245 °C annealed samples):

$$N_{\text{slow}} = N_{\text{atom}}(n_{\text{Ge}} - 0.25)\Phi(n_{\text{Ge}} - 0.25), \quad (30)$$

where N_{atom} is the atomic density and $\Phi(x)$ is the Heaviside step function. We can now solve Eq. (29) for the unknown energy factors, with the following result:

$$E_{\text{ani}} \text{sech}\left(\frac{E_{\text{slow}}}{k_B T}\right) = \sqrt{\left[\frac{d(CF(T))}{dn_{\text{Ge}}}\right] \frac{8M_s k_B T}{|\gamma|N_{\text{atom}}}}; \quad n_{\text{Ge}} > 0.25. \quad (31)$$

Substituting known parameter values, and remembering that $0 < \text{sech}(x) \leq 1$, we can determine a lower bound for the impurity exchange anisotropy as $E_{\text{ani}} \geq 2.7$ meV. We note that the exchange integral for transition-metal ferromagnets is of the order of 100 meV. In addition, the anisotropic exchange between the 4f moments of various rare earth ions and the Fe^{3+} spins in YIG is approximately 2 meV.⁶⁶ Thus, the order of magnitude for our estimated exchange-coupled anisotropy for the Ge atoms at the assumed impurity concentration, while not definitive, is well within the range of plausibility.

VII. CONCLUSION

We have presented results obtained by perpendicular VNA-FMR measurements on CMG samples for varying Ge content and annealing temperatures. Landau–Lifshitz damping plus inhomogeneous broadening alone cannot describe the damping in this material for all annealing temperatures and Ge contents. We found it necessary to add two additional terms: a low-field-loss term, and a “slow-relaxing” impurity-damping term. With these additions, the model can describe the entire frequency dependence of the linewidth. Moreover, the samples annealed at 245 and 300 °C exhibit a Landé g -factor that decreases linearly with increasing Ge content. The onset of slow-relaxer damping is correlated with the reduction of g below 2. Analysis of both magnetometry data in the context of GSP theory, as well as spectroscopic data for the dependence of g on Ge content, reveals that there is a significant spin polarization at the Ge sites that are antiferromagnetically coupled to the rest of the sample moment. The correlation of the amplitude of slow-relaxer damping, with Ge content for those samples where $g < 2$, suggests that some portion of the Ge sites act as the slow-relaxing “impurities” that lead to frequency-dependent damping, though the detailed energetics of the absorption mechanism are not yet understood. An understanding of the origin of the slow-relaxer damping might allow us to tune the damping in Heusler alloys to a desired value; i.e., either suppress it for spin-torque applications or enhance it for sensor applications.

ACKNOWLEDGMENTS

We acknowledge helpful discussions with Bret Heinrich, Martha Pardavi-Hovarth (George Washington University), Pavol Krivosik (University of Colorado at Colorado Springs), Mingzhong Wu (Colorado State University), and Pavel Kabos (National Institute of Standards and Technology). We also express our sincere gratitude to Tim and Claudia Mewes (University of Alabama at Tuscaloosa) for their useful observations and hypotheses concerning anomalous damping properties in Heusler alloys. We are also grateful for the many constructive editorial comments of the manuscript provided by Mark Keller (National Institute of Standards and Technology), Pavol Krivosik (University of Colorado at Colorado Springs), and John Read (Hitachi Global Storage Technologies). We thank S. Chandrashekariaih (Hitachi Global Storage Technologies) for assistance with sample preparation.

¹F. Heusler, *Verh. Dtsch. Phys. Ges.* **5**, 219 (1903).

²J. Kubler, A. R. Williams, and C. B. Sommers, *Phys. Rev. B* **28**, 1745 (1983).

³S. Picozzi, A. Continenza, and A. J. Freeman, *Phys. Rev. B* **66**, 094421 (2002).

⁴T. Taira, T. Ishikawa, N. Itabashi, K.-i. Matsuda, T. Uemura, and M. Yamamoto, *J. Phys. D: Appl. Phys.* **42**, 084015 (2009).

⁵Y. Sakuraba, M. Hattori, M. Oogane, Y. Ando, H. Kato, A. Sakuma, T. Miyazaki, and H. Kubota, *Appl. Phys. Lett.* **88**, 192508 (2006).

⁶T. Taira, T. Ishikawa, N. Itabashi, K.-i. Matsuda, T. Uemura, and M. Yamamoto, *Appl. Phys. Lett.* **94**, 072510 (2009).

⁷K. Inomata, N. Ikeda, N. Tezuka, R. Goto, S. Sugimoto, M. Wojcik, and E. Jedryka, *Sci. Technol. Adv. Mater.* **9**, 014101 (2008).

⁸T. Kubota, S. Tsunegi, M. Oogane, S. Mizukami, T. Miyazaki, H. Naganuma, and Y. Ando, *Appl. Phys. Lett.* **94**, 122504 (2009).

⁹J. R. Childress, M. J. Carey, S. Maat, N. Smith, R. E. Fontana, D. Druist, K. Carey, J. A. Katine, N. Robertson, T. D. Boone,

- M. Alex, J. Moore, and C. H. Tsang, *IEEE Trans. Magn.* **44**, 90 (2008).
- ¹⁰K. Nikolaev, P. Kolbo, T. Pokhil, X. Peng, Y. Chen, T. Ambrose, and O. Mryasov, *Appl. Phys. Lett.* **94**, 222501 (2009).
- ¹¹K. Kodama, T. Furubayashi, H. Sukegawa, T. M. Nakatani, K. Inomata, and K. Hono, *J. Appl. Phys.* **105**, 07E905 (2009).
- ¹²K. Yakushiji, K. Saito, S. Mitani, K. Takanashi, Y. K. Takahashi, and K. Hono, *Appl. Phys. Lett.* **88**, 222504 (2006).
- ¹³S. Fujii, S. Sugimura, Ishida, and S. Asano, *J. Phys. Cond. Matt.* **2**, 8583 (1990).
- ¹⁴I. Galanakis, P. H. Dederichs, and N. Papanikolaou, *Phys. Rev. B* **66**, 174429 (2002).
- ¹⁵H. C. Kandpal, G. H. Fecher, and C. Felser, *J. Phys. D: Appl. Phys.* **40**, 1507 (2007).
- ¹⁶P. J. Webster, *J. Phys. Chem. Solids* **32**, 1221 (1971).
- ¹⁷B. Rameev, F. Yildiz, S. Kazan, B. Aktas, A. Gupta, L. Tagirov, D. Rata, A. Buegler, P. Gruenberg, C. Schneider, S. Kammerer, G. Reiss, and A. Hutten, *Phys. Status Solidi A* **203** 1503 (2006).
- ¹⁸R. Yilgin, M. Oogane, Y. Ando, and T. Miyazaki, *J. Magn. Magn. Mater.* **310**, 2322 (2007).
- ¹⁹M. Belmeguenai, F. Zighem, G. Woltersdorf, Y. Roussigne, S. M. Cherif, K. Westerholt, and G. Bayreuther, *J. Magn. Magn. Mater.* **321**, 750 (2009).
- ²⁰M. Belmeguenai, F. Zighem, Y. Roussigné, S.-M. Chérif, P. Moch, K. Westerholt, G. Woltersdorf, and G. Bayreuther, *Phys. Rev. B* **79**, 024419 (2009).
- ²¹S. Mizukami, D. Watanabe, M. Oogane, Y. Ando, Y. Miura, M. Shirai, and T. Miyazaki, *J. Appl. Phys.* **105**, 07D306 (2009).
- ²²H. Lee, Y.-H. A. Wang, C. K. A. Mewes, W. H. Butler, T. Mewes, S. Maat, B. York, M. J. Carey, and J. R. Childress, *Appl. Phys. Lett.* **95**, 082502 (2009).
- ²³G. M. Muller, J. Walowski, M. Djordjevic, G.-X. Miao, A. Gupta, A. V. Ramos, K. Gehrke, V. Moshnyaga, K. Samwer, J. Schmalhorst, A. Thomas, A. Hutten, G. Reiss, J. S. Moodera, and M. Munzenberg, *Nat. Mater.* **8**, 56 (2009).
- ²⁴Y. Liu, L. R. Shelford, V. V. Kruglyak, R. J. Hicken, Y. Sakuraba, M. Oogane, and Y. Ando, *Phys. Rev. B* **81**, 094402 (2010).
- ²⁵C. Liu, C. K. A. Mewes, M. Chshiev, T. Mewes, and W. H. Butler, *Appl. Phys. Lett.* **95**, 022509 (2009).
- ²⁶R. D. McMichael and P. Krivosik, *IEEE Trans. Magn.* **40** 2 (2004).
- ²⁷J. H. Van Vleck and R. Orbach, *Phys. Rev. Lett.* **11**, 65 (1963).
- ²⁸A. Rajanikanth, Y. K. Takahashi, and K. Hono, *J. Appl. Phys.* **101**, 023901 (2007).
- ²⁹M. J. Carey, S. Maat, S. Chandrashekariiah, J. A. Katine, W. Chen, B. York, P. Vanderheijden, and J. R. Childress, *J. Appl. Phys.* **109**, 093912 (2011).
- ³⁰B. A. Collins, Y. Zhong, Y. S. Chu, L. He, and F. Tsui, *J. Vac. Sci. Technol. B* **25**, 999 (2007).
- ³¹T. Ambrose and O. Mryasov, *Lect. Notes Phys.* **676**, 187 (2005).
- ³²T. Ishikawa, T. Marukame, K.-i. Matsuda, T. Uemura, M. Arita, and M. Yamamoto, *J. Appl. Phys.* **99**, 08J110 (2006).
- ³³T. Graf, F. Casper, J. Winterlik, B. Balke, G. H. Fecher, and C. Felser, *Z. Anorg. Allg. Chem.* **635**, 976 (2009).
- ³⁴I. Neudecker, G. Woltersdorf, B. Heinrich, T. Okuno, G. Gubbiotti, and C. H. Back, *J. Magn. Magn. Mater.* **307**, 148 (2006).
- ³⁵S. S. Kalarickal, P. Krivosik, M. Wu, C. E. Patton, M. L. Schneider, P. Kabos, T. J. Silva, and J. P. Nibarger, *J. Appl. Phys.* **99**, 093909 (2006).
- ³⁶Y. Ding, T. J. Klemmer, and T. M. Crawford, *J. Appl. Phys.* **96**, 2969 (2004).
- ³⁷G. Council, J.-V. Kim, T. Devolder, C. Chappert, K. Shigeto, and Y. Otani, *J. Appl. Phys.* **95**, 5646 (2004).
- ³⁸M. L. Schneider, J. M. Shaw, A. B. Kos, T. Gerrits, T. J. Silva, and R. D. McMichael, *J. Appl. Phys.* **102**, 103909 (2007).
- ³⁹W. H. Press, B. P. Flannery, S. A. Teukolsky, and W. T. Vetterling, *Numerical Recipes in C: The Art of Scientific Computing* (Cambridge University Press, 1992).
- ⁴⁰B. Heinrich, J. F. Cochran, and R. Hasegawa, *J. Appl. Phys.* **57**, 3690 (1985).
- ⁴¹H. Chen, P. D. Gasperis, R. Marcelli, M. Pardavi-Horvath, R. McMichael, and P. E. Wigen, *J. Appl. Phys.* **67**, 5530 (1990).
- ⁴²M. Sparks, *J. Appl. Phys.* **38**, 1031 (1967).
- ⁴³J. F. Dillon and J. W. Nielsen, *Phys. Rev. Lett.* **3**, 30 (1959).
- ⁴⁴G. Woltersdorf, M. Kiessling, G. Meyer, J.-U. Thiele, and C. H. Back, *Phys. Rev. Lett.* **102**, 257602 (2009).
- ⁴⁵H. B. Callen and T. A. Welton, *Phys. Rev.* **83**, 34 (1951).
- ⁴⁶R. Kubo, *J. Phys. Soc. Jpn.* **12**, 570 (1957).
- ⁴⁷A. Rebei and G. J. Parker, *Phys. Rev. B* **67**, 104434 (2003).
- ⁴⁸R. Kubo, *Rep. Prog. Phys.* **29**, 255 (1966).
- ⁴⁹W. F. Brown, *Phys. Rev.* **130**, 1677 (1963).
- ⁵⁰T. J. Silva and M. W. Keller, *IEEE Trans. Magn.* **46**, 3555 (2010).
- ⁵¹E. Schloemann, *IEEE Trans. Magn.* **28**, 3300 (1992).
- ⁵²R. Urban, G. Woltersdorf, and B. Heinrich, *Phys. Rev. Lett.* **87**, 217204 (2001).
- ⁵³Y. Tserkovnyak, A. Brataas, and G. E. W. Bauer, *Phys. Rev. Lett.* **88**, 117601 (2002).
- ⁵⁴T. Gerrits, M. L. Schneider, and T. J. Silva, *J. Appl. Phys.* **99**, 023901 (2006).
- ⁵⁵K. H. J. Buschow, *Rep. Prog. Phys.* **40**, 1179 (1977).
- ⁵⁶H.-S. Li, Y. P. Li, and J. M. D. Coey, *J. Phys. Cond. Matt.* **3**, 7277 (1991).
- ⁵⁷I. Galanakis, *Phys. Rev. B* **71**, 012413 (2005).
- ⁵⁸S. Wurmehl, G. H. Fecher, H. C. Kandpal, V. Ksenofontov, C. Felser, H.-J. Lin, and J. Morais, *Phys. Rev. B* **72**, 184434 (2005).
- ⁵⁹G. H. Fecher, H. C. Kandpal, S. Wurmehl, C. Felser, and G. Schonhense, *J. Appl. Phys.* **99**, 08J106 (2006).
- ⁶⁰J. Kuebler, *Physica B + C (Amsterdam)* **127B**, 257 (1984).
- ⁶¹A. P. Malozemoff, A. R. Williams, and V. L. Moruzzi, *Phys. Rev. B* **29**, 1620 (1984).
- ⁶²K. Miyamoto, A. Kimura, K. Iori, K. Sakamoto, T. Xie, T. Moko, S. Qiao, M. Taniguchi, and K. Tsuchiya, *J. Phys. Cond. Matt.* **16**, S5797 (2004).
- ⁶³M. Sargolzaei, M. Richter, K. Koepernik, I. Opahle, H. Eschrig, and I. Chaplygin, *Phys. Rev. B* **74**, 224410 (2006).
- ⁶⁴A. Nefedov, J. Grabis, A. Bergmann, K. Westerholt, and H. Zabel, *Phys. B: Cond. Matt.* **345**, 250 (2004).
- ⁶⁵S. Maat, M. J. Carey, S. Chandrashekariiah, J. Katine, X. Liu, N. Smith, P. Vanderheijden, K. Vo, and J. R. Childress, *Intermag 2009 Digest*, EA-03 (2009).
- ⁶⁶M. Sparks, *Ferromagnetic-Relaxation Theory* (McGraw-Hill, New York, 1964).